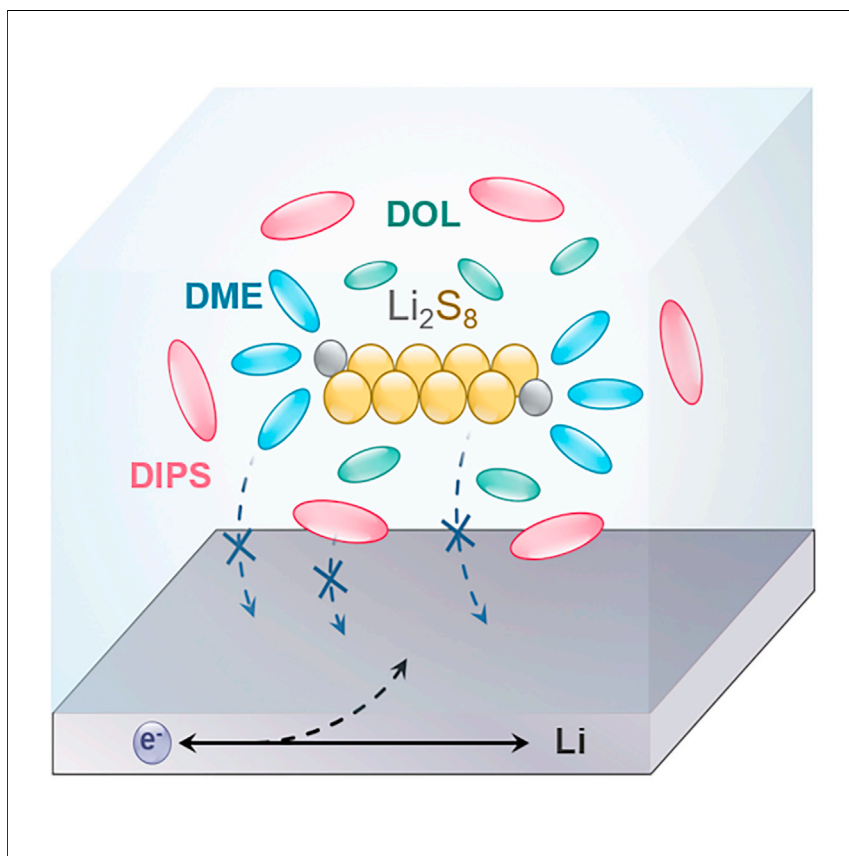


Article

An encapsulating lithium-polysulfide electrolyte for practical lithium–sulfur batteries



An encapsulating LiPS electrolyte (EPSE) is proposed for suppression of parasitic reactions based on a nano-heterogeneous solvation structure design of LiPSs. In the EPSE with di-isopropyl sulfide (DIPS) as a co-solvent, soluble LiPSs are encapsulated into two concentric solvent shells with different solvating power and reduction stability. Reduction-stable DIPS in the outer solvent shell significantly suppresses the parasitic reactions between encapsulated LiPSs and lithium metal. This work opens up new frontiers in electrolyte engineering toward long-cycling lithium–sulfur batteries.

Li-Peng Hou, Xue-Qiang Zhang, Nan Yao, ..., Cheng-Bin Jin, Jia-Qi Huang, Qiang Zhang

zhangxq@bit.edu.cn (X.-Q.Z.)
zhang-qiang@mails.tsinghua.edu.cn (Q.Z.)

Highlights

A nano-heterogeneous solvation structure of lithium polysulfides is investigated

An encapsulating LiPS electrolyte (EPSE) is designed for lithium–sulfur batteries

A 1.2 Ah pouch cell under demanding conditions undergoes 103 cycles in an EPSE

Two crucial criteria for constructing the EPSE are proposed

Article

An encapsulating lithium-polysulfide electrolyte for practical lithium–sulfur batteries

Li-Peng Hou,¹ Xue-Qiang Zhang,^{2,3,*} Nan Yao,¹ Xiang Chen,¹ Bo-Quan Li,^{2,3} Peng Shi,¹ Cheng-Bin Jin,¹ Jia-Qi Huang,^{2,3} and Qiang Zhang^{1,4,*}

SUMMARY

Practical lithium–sulfur batteries are severely hindered by parasitic reactions between lithium metal anodes and soluble lithium polysulfide (LiPS) intermediates. The solvation structure of LiPSs is pivotal in dictating the reaction kinetics. Herein, an encapsulating LiPS electrolyte (EPSE) is proposed to suppress parasitic reactions based on a nano-heterogeneous solvation structure design of LiPSs. In EPSE, with di-isopropyl sulfide (DIPS) as a co-solvent, soluble LiPSs are encapsulated into two concentric solvent shells with different solvating power and reduction stability. Reduction-stable DIPS in the outer solvent shell significantly suppresses the parasitic reactions between encapsulated LiPSs and lithium metal. A 1.2 Ah pouch cell under demanding conditions undergoes 103 cycles in the EPSE. This work provides two crucial criteria for constructing EPSE, that is, poor solvating power and high reduction stability of the solvent in outer solvent shell, and it opens up new frontiers in modulating the solvation structure of LiPSs toward long-cycling lithium–sulfur batteries.

INTRODUCTION

Lithium–sulfur (Li–S) batteries have gained momentum as a promising energy-storage system endowed with a high theoretical energy density of 2,600 Wh kg^{−1} and the employment of earth-abundant S as the cathode.¹ A working Li–S battery undergoes a multistep solid–liquid–solid conversion of the S cathode involving Li polysulfide (LiPS) intermediates. Soluble LiPSs act as important inherent redox mediators to stimulate the conversion kinetics of the S cathode, ensuring the high specific energy of Li–S batteries.² However, LiPSs in electrolyte are highly active and can parasitically react with Li metal anodes.³ During cycling, active Li is continuously exposed to and reacts with LiPSs owing to the rupture of the solid electrolyte interphase (SEI) by large volume fluctuation in plating/stripping processes. The parasitic reactions between LiPSs and Li metal anodes deplete limited Li reservoirs^{4,5} and form parasitic products on Li metal surfaces,^{6,7} accelerating the accumulation of dead Li and inducing rapid failure of Li–S batteries. When it comes to practical Li–S batteries with demanding operation conditions, the parasitic reactions are aggressive.^{8,9} Under demanding conditions with a low electrolyte/sulfur (E/S) ratio (<3 μL mg^{−1}), the concentration of LiPSs increases from <3 M total S species ([S]) to >6 M [S]. The amount of utilized Li in each cycle increases from <2 to >5 mAh cm^{−2} (about 50% of pristine Li), and the reactive specific surface area of Li extends significantly. High-concentration LiPSs and high specific-surface-area Li aggressively intensify the parasitic reactions and thus the rapid depletion of limited Li reservoir (<50 μm).^{10–12} Therefore, the detrimental parasitic reactions must be overcome to prolong the cycling of practical Li–S batteries.

The bigger picture

The pursuit of a zero-carbon and wireless society necessitates the development of high-energy-density and long-cycling batteries as the power source for portable electronics, electric vehicles, and so on. The lithium–sulfur battery is a promising high-energy-density battery system. However, parasitic reactions between lithium metal anodes and soluble lithium polysulfide (LiPS) intermediates severely hinder the lifespans of practical lithium–sulfur batteries, and rational electrolyte design is imperative. Herein, an encapsulating LiPS electrolyte (EPSE) is designed based on an insightful understanding of the solvation structure of LiPSs, which mitigates the parasitic reaction kinetics and significantly improves the cycle life of practical lithium–sulfur batteries. This opens up new frontiers in electrolyte design toward long-cycling lithium–sulfur batteries.



The reaction kinetics regulation is pivotal to the inhibition of the parasitic reactions between LiPSs and Li metal anodes. Decreasing the concentration of LiPSs in electrolyte is a conventional wisdom. Physical confinement and chemical adsorption at the cathode side to block the diffusion of LiPSs^{13,14} and electro-/chemical catalysis^{15–18} to accelerate the liquid–solid conversion of LiPSs have been widely employed to indirectly mitigate the parasitic reactions by decreasing the concentration of dissolved LiPSs. However, the effectiveness of these strategies under practical conditions is still challenged.¹² Electrolyte design is also employed to decrease LiPS concentration, in which sparingly solvating electrolytes have great promise. In sparingly solvating electrolytes, the solubility of LiPSs is reduced to an extremely low level (generally <50 mM [S] compared with >6 M [S] in routine ether-based electrolytes) through the increased salt concentrations or introduction of low polar solvents.¹⁹ The current sparingly solvating electrolytes include solvent-in-salt electrolytes,²⁰ localized high-concentration electrolytes,^{21,22} and solvated ionic-liquid electrolytes.^{23,24} However, the conversion-reaction kinetics of S cathodes in sparingly solvating electrolytes are dramatically altered due to the insufficient supply of LiPSs as inherent redox mediators.^{25,26} An extremely decreased LiPS concentration triggers a sluggish quasi-solid or solid–solid conversion mechanism, losing the advantage of high utilization of S based on a solid–liquid–solid conversion mechanism. Suppressing the parasitic reactions but compromising the kinetics of S conversion abandons the attraction of high specific energy of Li–S batteries. Consequently, new regulation methodologies of reaction kinetics of LiPSs in electrolytes are imperative to break through the dilemma of suppressing the parasitic reactions on Li metal anodes but compromising the kinetics of S conversion.

In addition to LiPS concentration, the surroundings of LiPSs in electrolyte play an essential role in dictating reaction kinetics.^{9,27,28} In working Li–S batteries, the surroundings of LiPSs mainly refer to the solvation structure of LiPSs. Polysulfide anions interact with Li ions via ion–ion interactions^{29,30} and Li ions can be solvated by solvent molecules through ion–dipole interactions.^{31,32} Hence, LiPSs are surrounded by solvent shells and the solvation structure of LiPSs depends on the solvating power of solvent molecules. Solvents with high solvating power, such as dimethylacetamide (DMA) and tetramethylurea (TMU), exhibit predominance in accelerating the liquid–liquid conversion and changing the liquid–solid nucleation patterns from two to three dimensions, which promotes the conversion kinetics of the S cathode.^{28,33,34} Inspiringly, the solvation structure of LiPSs is supposed to be regulated to decrease the parasitic reaction kinetics on Li metal anodes, although the related research has been insufficient until now. Naturally, a design of nano-heterogeneous solvent shells is conceived by regulating the interactions of solvent molecules with LiPSs. An inner solvent shell with high solvating power is necessary to dissolve certain LiPSs and ensure the cathode conversion kinetics. An outer solvent shell with poor solvating power and high reduction stability is ideally indispensable to mitigate the parasitic reaction kinetics of the dissolved LiPSs on the Li metal anode. Therefore, the design of nano-heterogeneous solvent shells is anticipated to suppress the parasitic reaction kinetics without the cost of cathode conversion kinetics in practical Li–S batteries.

In this contribution, an encapsulating LiPS electrolyte (EPSE) is demonstrated as the design of nano-heterogeneous solvent shells, which mitigates the parasitic reactions between the Li metal anode and the LiPS electrolyte without a cost of cathode conversion kinetics. The EPSE is achieved by employing a thioether with poor solvating power and high reduction stability, di-isopropyl sulfide (DIPS), to regulate the solvation structure of LiPSs. LiPSs are encapsulated into two concentric solvent shells in

¹Beijing Key Laboratory of Green Chemical Reaction Engineering and Technology, Department of Chemical Engineering, Tsinghua University, Beijing 100084, P.R. China

²Advanced Research Institute of Multidisciplinary Science, Beijing Institute of Technology, Beijing 100081, P.R. China

³School of Materials Science and Engineering, Beijing Institute of Technology, Beijing 100081, P.R. China

⁴Lead contact

*Correspondence: zhangxq@bit.edu.cn (X.-Q.Z.), zhang-qiang@mails.tsinghua.edu.cn (Q.Z.)
<https://doi.org/10.1016/j.chempr.2021.12.023>

EPSE, proved by molecular dynamics (MD) simulations and nuclear magnetic resonance (NMR) measurements. The inner solvent shell with high solvating power ensures the satisfactory conversion kinetics of the S cathode. DIPS with a weak solvating power appears in the outer solvent shell to encapsulate the centered LiPSs. The high reduction stability of the outer solvent shell endows the mitigated kinetics of parasitic reactions on Li metal anodes. The solvating power and reduction stability of the outer-shell solvents are recognized as two basic criteria for achieving the EPSE. A 1.2 ampere hour (Ah) level pouch cell with the EPSE delivers 103 cycles, which is a pioneering report in Li–S pouch cells resulting from mere electrolyte design. The disassembly analysis of the cycled pouch cell is further disclosed.

RESULTS

The construction of the EPSE

The nano-heterogeneous solvent shells with different solvating power and reduction stability are the key to construct the EPSE. In order to dissolve LiPSs and ensure S conversion reaction kinetics, routine ethers with high solvating power, such as 1,2-dimethoxyethane (DME), are superior candidates for the inner solvent shell, which has been realized in the previous reports.^{32,35} The crux to mitigating the parasitic reactions is choosing qualified solvent molecules with poor solvating power and high reduction stability to construct the outer solvent shell of LiPSs. The DIPS molecule is selected due to the low coordination ability of S atoms and the large steric hindrance of isopropyl. First, the LiPS solubility of DIPS is evaluated. 10.0 mM Li_2S_8 was stirred into pure DIPS solvent for 48 h. The solution is colorless and no signal of polysulfides is detected by ultraviolet-visible (UV-vis) spectroscopy, indicating that Li_2S_8 is not dissolved in DIPS (Figure S1). Other typical LiPS species are also insoluble in DIPS due to the decreased solubility with a shorter chain length of LiPSs.³⁰ In sharp contrast, LiPSs have a high solubility in mixed 1,3-dioxolane (DOL)/DME solvent with over 6 M [S].^{8,9} Despite the difference in LiPS solubility, DIPS is miscible with DOL and DME. 1.0 M lithium bis-(trifluoromethanesulfonyl) imide (LiTFSI) can be dissolved into a mixed solvent of DIPS/DOL/DME (1:2:2, by vol.) and the electrolyte obtained is denoted as DIPS-EPSE. The routine ether-based electrolyte 1.0 M LiTFSI dissolved in DOL/DME (1:1, by vol.) is denoted as DOL/DME. The significant difference in the solubility of LiPSs and the miscibility between DIPS and routine ethers indicate that DIPS is capable of constructing the outer solvent shell of LiPSs. Second, reduction stability is an important parameter. DIPS possesses better reduction stability against Li metal than pure DOL and DME with a much lower current response in cyclic voltammogram test (Figure S2). The stability against Li metal of DIPS-EPSE without LiPSs is assessed in Li | Li symmetric cells (Figure S3). The polarization voltage of the Li | Li symmetric cell with DIPS-EPSE maintains relatively stability during the 400-h test (increased by 160 mV). In comparison, the Li | Li symmetric cell with DOL/DME displays a dramatically increased polarization voltage after 300 h, which is up to 950 mV at 340 h. Consequently, DIPS is a qualified candidate solvent to construct the outer solvent shell of LiPSs and achieve the design of EPSE for mitigating the parasitic reactions.

The alleviated parasitic reactions between LiPS electrolyte and Li metal in DIPS-EPSE are verified by an optical experiment. A fresh Li foil was directly immersed into DIPS-EPSE or DOL/DME containing 1.0 mM Li_2S_8 . The components in solutions were detected by *in situ* UV-vis spectroscopy (Figure 1A). The absorbance of the absorption shoulder peak at 420 nm (S_4^{2-}) decreases from 1.4 to 0.6 dramatically in DOL/DME with Li_2S_8 after 10 h.^{36,37} In comparison, the absorbance at 420 nm remains steady at 1.0 in DIPS-EPSE, indicating that LiPSs in DIPS-EPSE are more stable

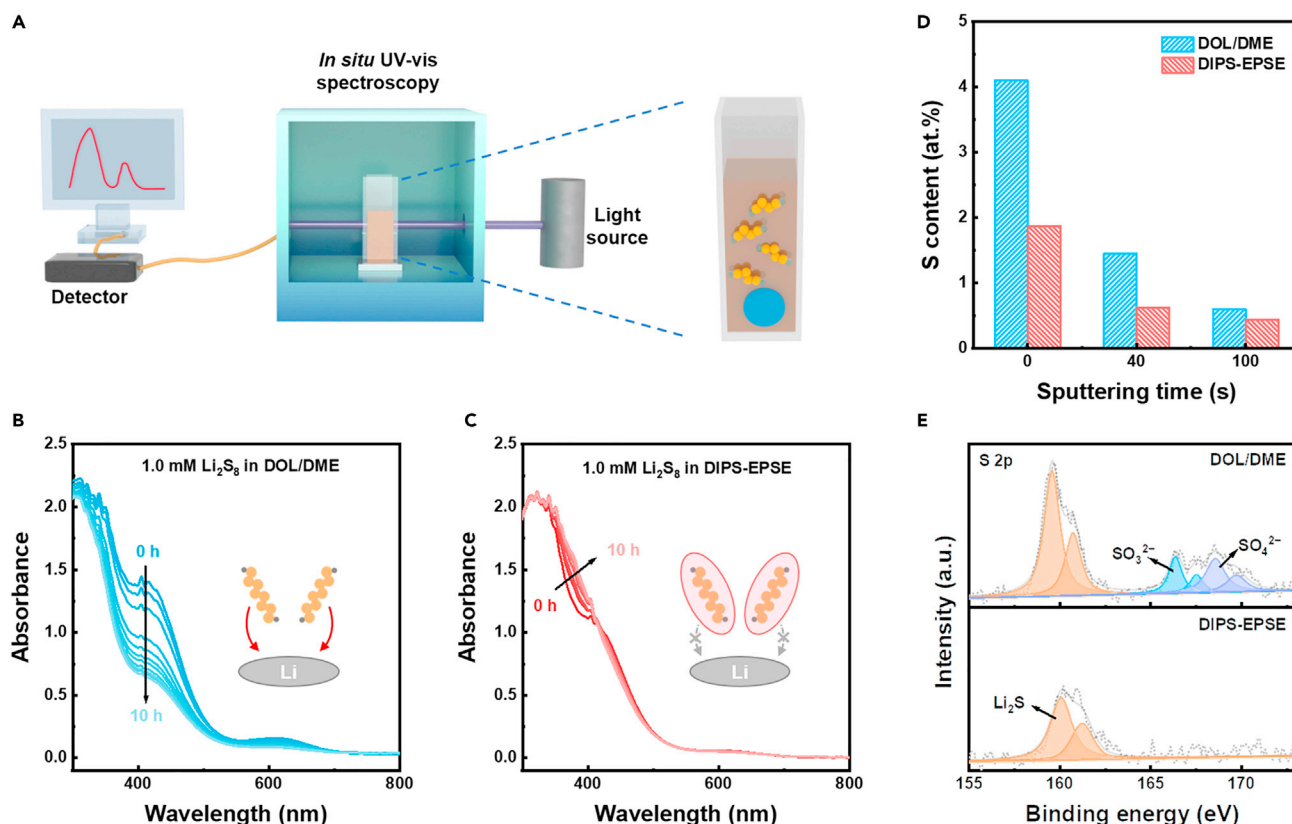


Figure 1. The characterization of parasitic reactions between LiPSs and the Li anode

(A) Schematic of the *in situ* UV-vis spectroscopy test.

(B and C) *In situ* UV-vis spectra of (B) DOL/DME and (C) DIPS-EPSE with 1.0 mM Li_2S_8 , in which fresh Li foils were immersed. The insets in (B) and (C) represent the different interactions between LiPSs and Li metal anodes in DOL/DME and DIPS-EPSE.

(D) The S atomic content on the surface of Li foils at different sputtering times (0, 40, and 100 s) after immersion in DOL/DME or DIPS-EPSE.

(E) XPS spectra of S 2p on the Li foil after immersion in DOL/DME or DIPS-EPSE after 40-s sputtering.

with Li metal anodes and less consumed (Figures 1B and 1C). Furthermore, a Li foil was immersed in DIPS-EPSE or DOL/DME containing 3.0 mM Li_2S_8 . The dark brown DOL/DME with Li_2S_8 faded to almost colorless within 24 h due to the parasitic reduction reactions of Li_2S_8 with Li metal (Figure S4), while DIPS-EPSE with Li_2S_8 remained yellow for 24 h, demonstrating the mitigated parasitic reactions. The solid reaction products between LiPS solutions and the Li metal were analyzed by in-depth X-ray photoelectron spectroscopy (XPS). The S atomic content on the Li foil surface in DIPS-EPSE was much lower than that in DOL/DME at different sputtering times (1.87% versus 4.10%, 0.62% versus 1.45%, and 0.44% versus 0.60% at 0, 40, and 100 s; Figure 1D). SO_4^{2-} , SO_3^{2-} , and Li_2S were detected on the Li surface in DOL/DME (sputtering 40 s) while only Li_2S was detected on the Li surface in DIPS-EPSE (Figure 1E). The Li foil in DOL/DME containing LiPSs was obviously corroded with discrete granular reaction products on the surface (Figure S5A). In contrast, the Li foil in DIPS-EPSE was much smoother under less destruction. Notably, 3.0 mM LiPSs in DIPS-EPSE and DOL/DME are fully dissolved but the parasitic reactions differ dramatically. In addition, the function of the SEI in shielding the parasitic reactions of LiPSs is excluded (Figures S6 and S7). The SEI chemically and electrochemically formed in DIPS-EPSE cannot inhibit the parasitic reactions of LiPSs. Therefore, it is the modulated solvation structure of LiPSs that mitigates the reactivity of LiPSs with Li metal anodes in DIPS-EPSE, implying the successful construction of the EPSE.

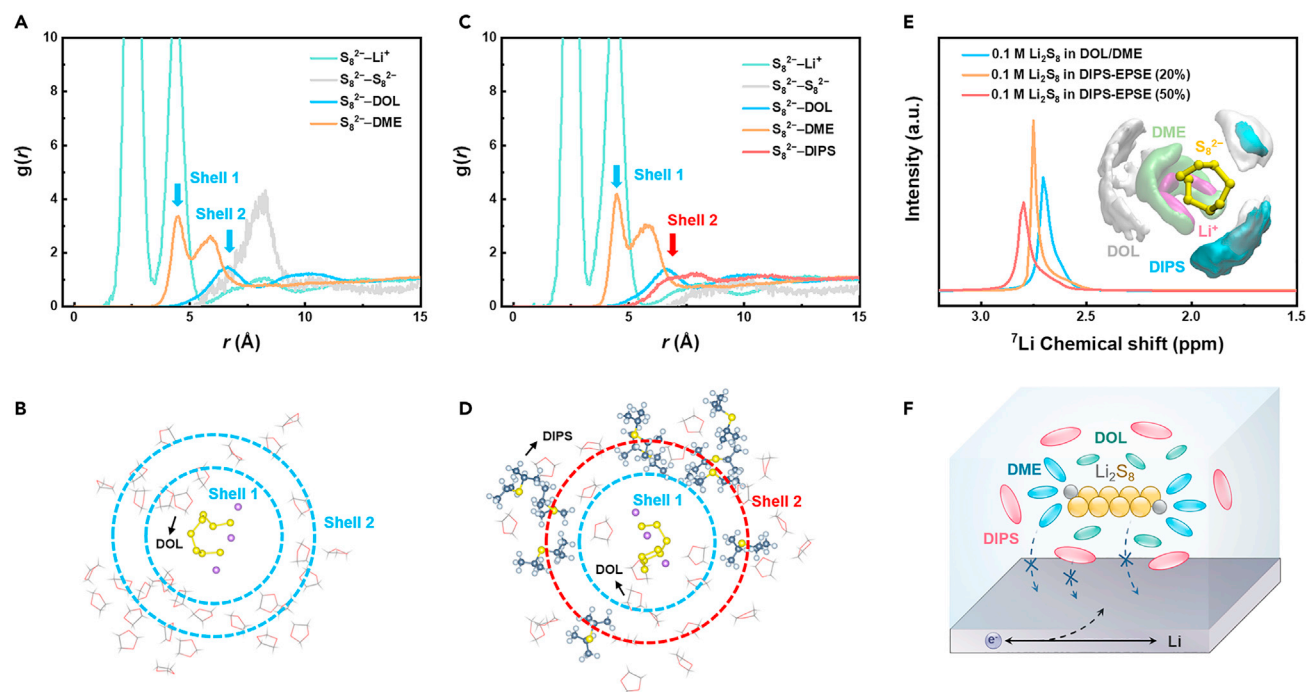


Figure 2. The solvation structure of LiPSs

(A and C) The radial distribution function ($g(r)$) around S_8^{2-} in (A) DOL/DME and (C) DIPS-EPSE. The radial distance (r) is from the center of mass of selected (S_8^{2-}) to other molecules (Li^+ , S_8^{2-} , DME, DOL, and DIPS). Shell 1 and shell 2 are the shells composed of solvents specifically according to the distance from the selected central S_8^{2-} .

(B and D) Snapshots of the molecular distributions around S_8^{2-} in (B) DOL/DME and (D) DIPS-EPSE. DME and TFSI⁻ are omitted for a clear comparison. (E) 7Li -NMR spectra of 0.1 M Li_2S_8 in DOL/DME and DIPS-EPSE. DOL/DME and DIPS-EPSE are pure solvent mixtures without LiTFSI. The illustration in (E) is the spatial distribution functions (SDFs) of DIPS-EPSE.

(F) Scheme of the solvation structure of DIPS-EPSE.

The solvation structure of LiPSs in the EPSE

MD simulations aid in decoding the solvation structure of LiPSs. 0.1 M LiPSs (Li_2S_8 , Li_2S_6 , or Li_2S_4) in DOL/DME or DIPS-EPSE were investigated. Because the reactivity of LiPSs is dependent on the chain length, Li_2S_8 is chosen as a typical example for detailed illustrations.³² In DOL/DME, centered on the S_8^{2-} , Li^+ interacts with S_8^{2-} strongly, with the shortest distance at 2.5 Å in DOL/DME, implying that S_8^{2-} appears in the solvation sheath of Li^+ (Figure 2A).^{30,38} Besides, there are two concentric solvent shells around S_8^{2-} through the bridge of $S_8^{2-}-Li^+$ -solvent interactions (Figures 2A and 2B). DME preferentially appears at the position of 4.5 Å from the center of S_8^{2-} and near Li^+ due to its strong solvating power, forming an inner solvent shell (shell 1). DOL molecules appear at the position of 6.6 Å and are recruited in the outer solvent shell (shell 2) due to their relatively weak solvating power. Shell 2 is composed of a mixture of DOL and DME, which wraps the inner solvent shell. DME is a crucial component in dissolving LiPSs to maintain the conversion reaction kinetics of the S cathode.^{39–41} However, Li ions are considered to reduce the lowest unoccupied molecular orbital (LUMO) level of DOL and DME solvents via ion–dipole interactions, exacerbating the decomposition of DOL and DME⁴² and exposing reactive LiPSs to corrode Li metal anodes. The introduction of DIPS into the routine electrolyte changes the solvation structure of LiPSs. In DIPS-EPSE, the inner solvent shell (shell 1) around the centered S_8^{2-} is still composed of DME (4.5 Å) to ensure the dissolution of LiPSs, but DIPS molecules emerge in the outer solvent shell (shell 2) at 6.6 Å together with DOL (Figures 2C and 2D). This can be attributed to the low solvating power of DIPS due to the low coordination ability of the S atom compared

with that of the O atom and the large steric hindrance of isopropyl (Figure S1). Consequently, the outer solvent shell with highly reduction-stable DIPS encapsulates the centered LiPSs and inner solvent shell to mitigate the parasitic reactions on the Li metal surface (Figure S2). In addition to Li_2S_8 , the solvent shells of Li_2S_6 and Li_2S_4 are disclosed in DOL/DME and DIPS-EPSE with similar conclusions that an encapsulating LiPS solvent shell is formed in DIPS-EPSE (Figures S8 and S9).

NMR measurements were employed to verify the conclusions drawn from MD simulations (Figure 2E). The Li^+ in LiPSs interacts with the O atom in DME and DOL through ion-dipole interactions. Hence, ^7Li -NMR was used to infer the electrolyte structure of LiPSs. Compared with 0.1 M Li_2S_8 in DOL/DME, the chemical shift of ^7Li moves downfield from 2.71 to 2.75 ppm in DIPS-EPSE (containing 20% DIPS but without LiTFSI). When the content of DIPS increases to 50% in the mixture of DOL/DME/DIPS, the chemical shift of ^7Li further moves to 2.80 ppm. The deshielding effect of Li ions results from decreasing the electron cloud density around Li^+ , implying the emergence of DIPS in the outer solvent shell due to the much weaker ion-dipole interaction between Li^+ and S atom in DIPS compared with Li^+ -O interactions in DME or DOL. The spatial distribution functions (SDFs) shown in Figure 2E visually exhibit the spatial distributions of DIPS, DME, and DOL around Li_2S_8 . Additionally, in DIPS-EPSE containing 1.0 M LiTFSI and 0.1 M Li_2S_8 , the chemical shift of ^7Li moves from 1.38 ppm (DOL/DME) to 1.45 ppm (Figure S10), indicating that DIPS can alter the solvation structure of LiPSs in the electrolyte containing Li salts.

From the above results of theoretical calculations and experiments, the solvation structure of LiPSs in the EPSE is disclosed. DIPS with a low solvating power tends to distribute in the outer solvent shell around LiPSs, and the inner solvent shell is dominated by DME (Figure 2F). The inner shell can dissolve LiPSs to ensure the conversion kinetics of the S cathode. The outer shell, composed of highly reduction-stable DIPS solvents, plays a vital part in stably encapsulating LiPSs to suppress the parasitic reactions on the Li metal anode. Additionally, DIPS cannot dissolve LiTFSI and the decomposition of Li salt is meanwhile retarded (Figure 1E), which will be a ground for the further regulation of the solvation structure of LiPSs and Li salts synergistically.

Electrochemical performance of EPSE without LiNO_3

To assess the performance of DIPS-EPSE on mitigating parasitic reactions in Li-S batteries, no LiNO_3 is employed in electrolytes. The shuttle current, as an indicator of the corrosion of LiPSs on the Li metal anode, is sharply reduced by at least 7 times in DIPS-EPSE compared with DOL/DME at varied potentiostatic voltages (Figure 3A). Furthermore, Li-S batteries were evaluated with an S loading of 1.1 mg cm^{-2} and an E/S ratio of $17.1 \text{ }\mu\text{L mg}_\text{S}^{-1}$. The discharge capacity in DOL/DME and DIPS-EPSE is similar at the 2nd cycle (1,005 versus 1,016 mAh g^{-1}), corresponding to a concentration of 1.1 M [S] (about 0.14 M Li_2S_8) that can be fully dissolved. However, the Coulombic efficiency (CE) of DIPS-EPSE is obviously higher than that of DOL/DME (90.9% versus 79.0%; Figure 3B), indicating that the parasitic reactions of LiPSs and Li metal anodes are mitigated in Li-S batteries when using DIPS-EPSE.

The mitigated parasitic reactions further influence the solid reaction products in the SEI, which were detected by XPS after the 5th cycle. The S atomic content in the SEI with DIPS-EPSE is lower than that with DOL/DME (1.54% versus 2.30%, 0.96% versus 2.03%, 0.59% versus 1.16%, and 0.55% versus 1.05%, at 0, 40, 100, and 160 s sputtering, respectively; Figure 3C). SO_4^{2-} and SO_3^{2-} are both detected at the top layer of the SEI in DOL/DME and DIPS-EPSE (Figures 3D and S11). After 100-s sputtering,

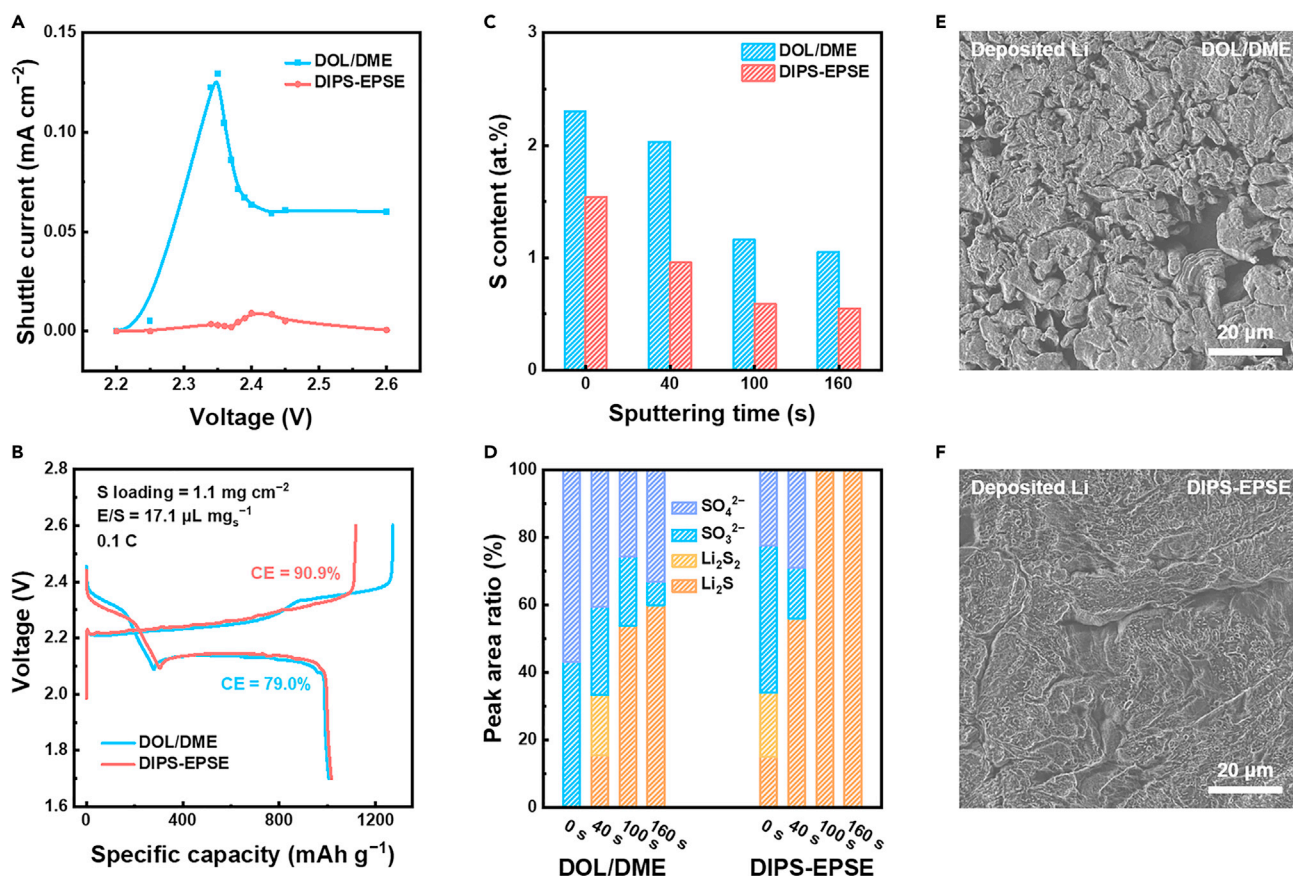


Figure 3. The electrochemical performance of Li-S batteries without LiNO_3

(A) Shuttle current at various potentiostatic charging voltages.
(B) Voltage-specific capacity profiles of Li-S coin cells.
(C) The S atomic content on the surface of Li metal anodes after the 5th cycle at a sputtering time of 0, 40, 100, and 160 s.
(D) The peak area ratio of S species on Li metal anodes after the 5th cycle at different sputtering times.
(E and F) The morphology of deposited Li after the 5th cycle in (E) DOL/DME and (F) DIPS-EPSE.

only Li_2S is detected in the SEI in DIPS-EPSE, while the S-containing species in a high oxidation state are still abundant in DOL/DME, implying that the decomposition of LiPSs and LiTFSI is alleviated due to the introduction of DIPS. The Li-ion transport behaviors in the SEI are further influenced, and different Li deposition morphologies are formed. Porous and dendritic Li is observed in DOL/DME (Figure 3E). In contrast, the Li deposition is dense and smooth in DIPS-EPSE (Figure 3F). In brief, the changed component distribution in the SEI demonstrates the alleviated parasitic reactions of DIPS-EPSE.

Li-S batteries under practical conditions

DIPS-EPSE was further evaluated in Li-S coin cells under practical conditions. An ultrathin Li anode (50 μm) and a high-loading S cathode (3.9 mg cm^{-2}) were employed with a theoretical N/P ratio of 1.6. The E/S ratio was set up at $7.7 \text{ } \mu\text{L mg}_\text{S}^{-1}$ considering the loss of partial electrolyte in the useless space in coin cells. LiNO_3 was employed to further improve the performance of Li-S batteries.^{43,44} The Li-S battery with DIPS-EPSE delivers an initial capacity of $1,180 \text{ mAh g}^{-1}$, close to that of $1,228 \text{ mAh g}^{-1}$ in DOL/DME at the first discharge process (0.05 C), corresponding to about 3.0 M [S] (Figures 4A and S12). The discharge capacity of Li-S batteries with DOL/DME rapidly decays after 50 cycles with a striking decrease of CE. In

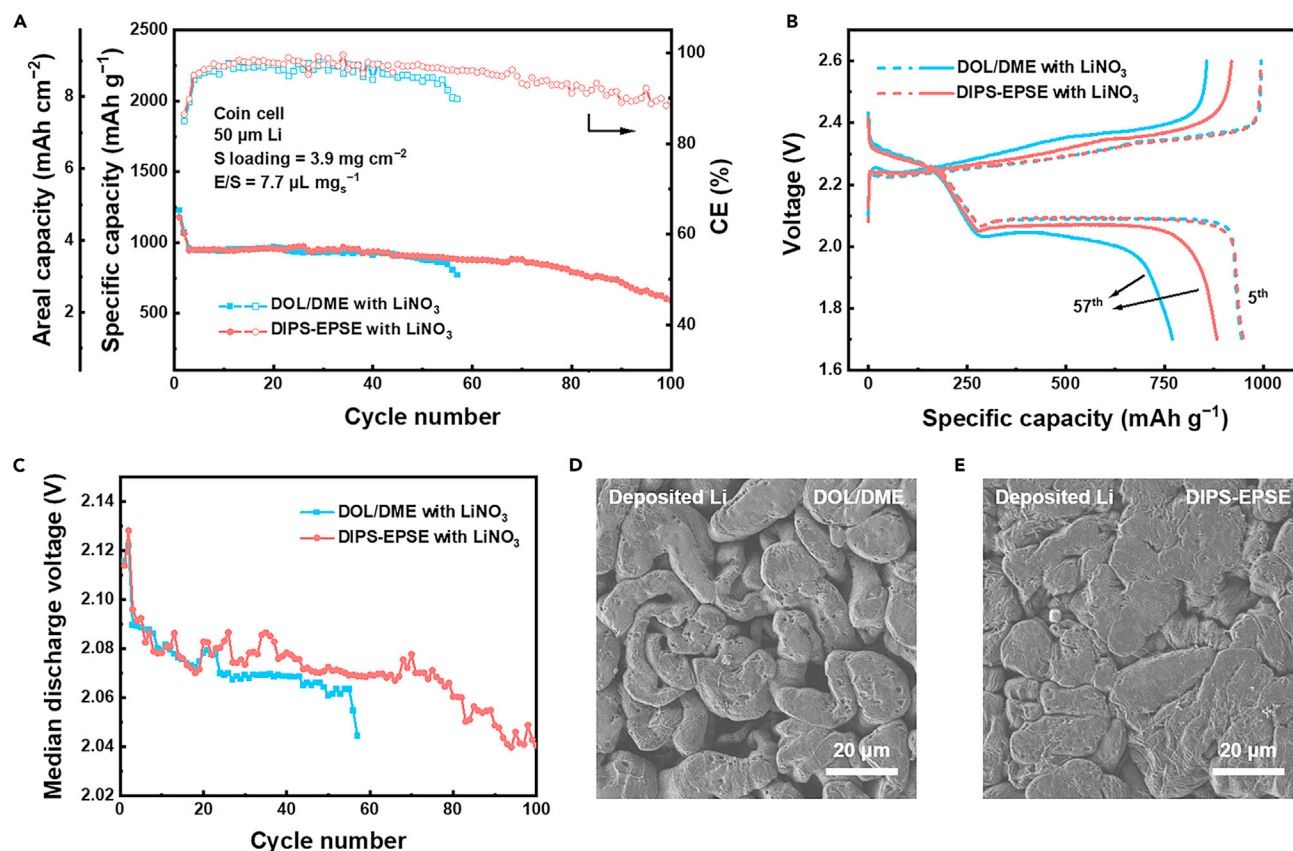


Figure 4. Electrochemical performance of Li-S batteries under practical conditions in coin cells

(A and B) Cycle performance of Li-S batteries under practical conditions and the corresponding voltage-specific capacity profiles at the 5th and 57th cycles at 0.1 C.

(C) Median discharge voltage of Li-S batteries during cycling.

(D and E) Li deposition morphologies of Li-S batteries after the 5th cycle in (D) DOL/DME and (E) DIPS-EPSE with the LiNO_3 additive.

contrast, the Li-S battery with DIPS-EPSE exhibits a stable operation for 100 cycles with a slow decay rate both in capacity and CE. The polarization profiles at the 5th cycle (0.1 C) in DIPS-EPSE are almost consistent with that in DOL/DME (Figure 4B), as is the capacity ratio between the first and second discharge plateaus (1:2.4), indicating that the conversion kinetics of the S cathode in DIPS-EPSE is acceptable compared with that in DOL/DME with a solid-liquid-solid conversion reaction. There is a dramatic increase in the polarization of the discharge curve of DOL/DME at the late stage at the 57th cycle, implying the inadequate Li supply and the accumulation of dead Li. However, the Li-S battery with DIPS-EPSE displays a smaller discharge polarization with a higher discharge capacity of 883 mAh g^{-1} compared with that in DOL/DME (770 mAh g^{-1}). The median discharge voltage of the Li-S battery with DIPS-EPSE is higher than that in DOL/DME after the initial 20 cycles, indicating a slower accumulation rate of dead Li and polarization (Figure 4C). The Li deposition morphology in DIPS-EPSE is smooth, opposite to aggressive Li dendrites in DOL/DME (Figures 4D and 4E). A higher portion of 25% DIPS in DIPS-EPSE also can achieve a better cycle stability of Li-S batteries for 90 cycles than DOL/DME but induce a reduction in discharge capacity of about 150 mAh g^{-1} at initial 20 cycles and inferior cycle performance compared with DIPS-EPSE with 20% DIPS (Figure S13). Moreover, the Li-S battery with DIPS-EPSE delivers superior rate performance with more stable CE and lower polarization than that with DOL/DME

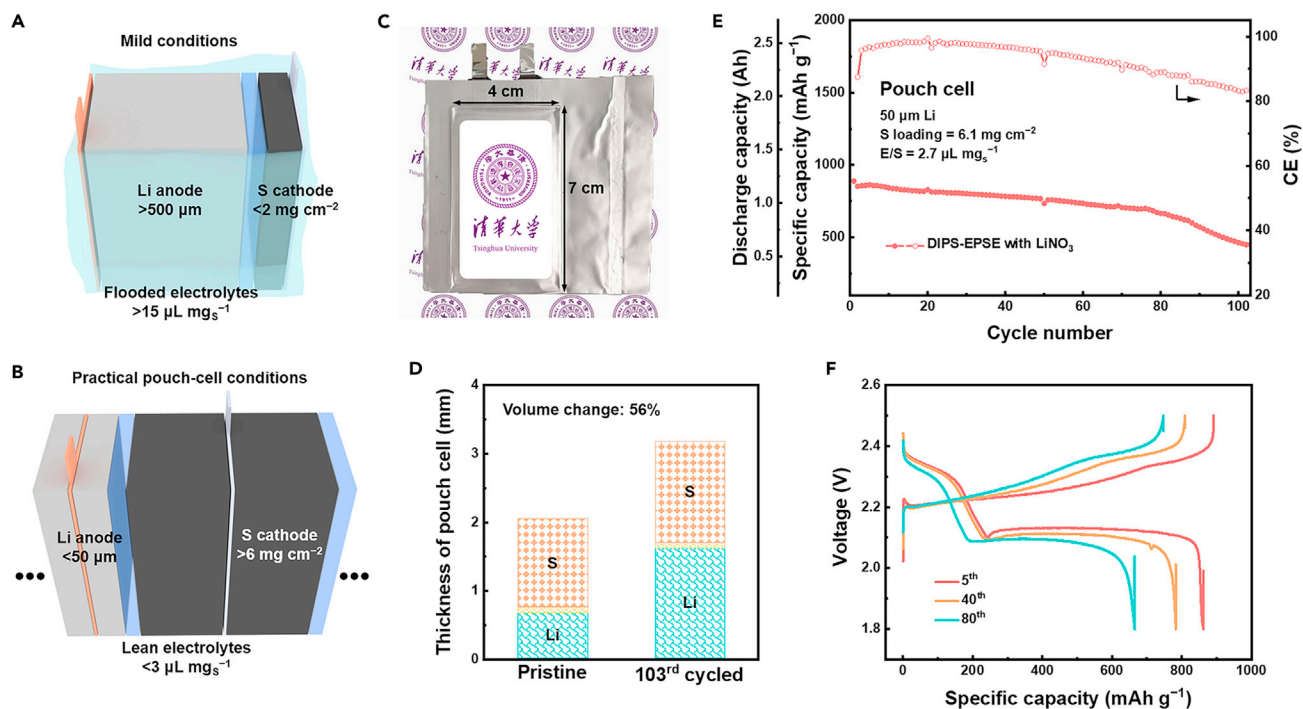


Figure 5. Cycling performance of a Li-S pouch cell using DIPS-EPSE containing LiNO_3

(A) Schematic of a Li-S battery under mild test conditions.

(B) Schematic of a Li-S pouch cell with demanding test conditions.

(C) Optical image of the practical Li-S pouch cell.

(D) The change of the total thickness of the pouch cell before and after 103 cycles.

(E and F) Cycle performance of the Li-S pouch cell and the corresponding voltage-specific capacity profiles at the 5th, 40th, and 80th cycle.

(Figure S14). On the basis of the above analysis, the mitigated parasitic reactions between Li metal anodes and LiPSs in DIPS-EPSE significantly improve the cycling performance of Li-S batteries under practical conditions.

Practical Li-S pouch cells

Compared with mild conditions for a proof of concept usually used in coin cells with a low S loading cathode (<2 mg cm^{-2}), flooded electrolytes ($\text{E/S} > 15 \mu\text{L g}^{-1}$), and an excessive amount of Li anodes (>500 μm), Li-S pouch cells were assembled to further evaluate the potential applications of DIPS-EPSE under practical conditions (Figures 5A and 5B). The Li anode, separator, and S cathode are arranged in stacks with a size of $7 \times 4 \text{ cm}^2$ (Figure 5C). Ultrathin Li metal anodes (50 μm), lean electrolytes (2.7 $\mu\text{L mg}_\text{S}^{-1}$), and high-loading S cathodes (6.1 mg cm^{-2}) are employed. The practical discharge capacity of the Li-S pouch cell is 1.2 Ah with an energy density of 325 Wh kg^{-1} (based on the mass of the whole pouch cell deducting the package). The pouch cell maintains a capacity retention of 50% after 103 cycles with an average CE of 93.0% (Figure 5E), which is a pioneering report in Li-S pouch cells under such harsh conditions using a mere electrolyte design. After 103 cycles, there is no gassing problem with a flat air pocket, while a severe gassing problem is recorded in routine ether-based electrolyte with the LiNO_3 additive according to the previous report.⁴⁵ The total thickness of the pouch cell changes from 2.04 to 3.18 mm with an expansion of 56% (Figure 5D), indicating a moderate volume expansion of the Li metal anode, considering that S cathodes also undergo volume fluctuation during cycling.^{46,47} The capacity ratio of the first and second discharge

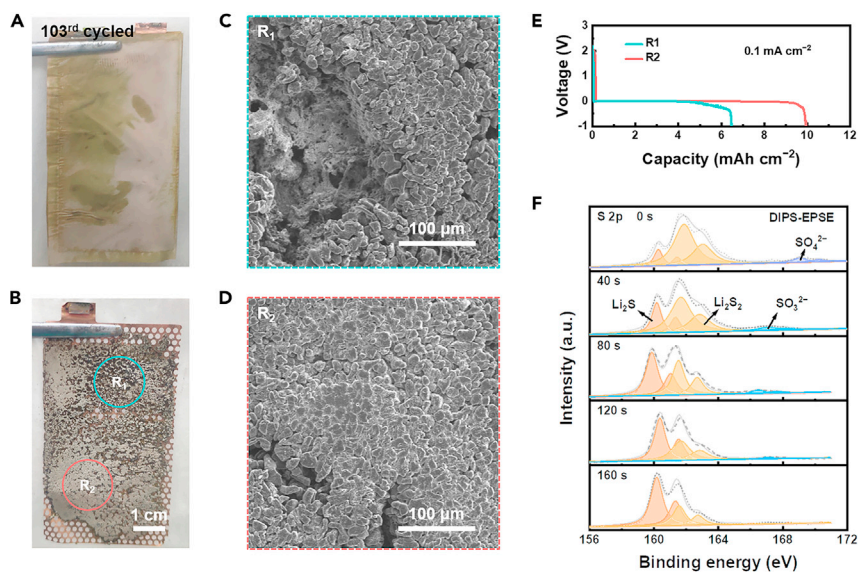


Figure 6. Analysis of the Li-S pouch cell using DIPS-EPSE containing LiNO₃ after 103 cycles

(A and B) Optical images of (A) the core of the battery and (B) the Li metal anode.

(C and D) SEM images of the cycled Li metal anode in various regions.

(E) Analysis of the residual amount of active Li in the cycled Li metal anode in various regions.

(F) XPS spectra of S 2p on the cycled Li metal anode.

plateaus is 1:2.6 at the 5th cycle, which is close to a theoretical capacity ratio of 1:3 and corresponds to a typical solid-liquid-solid conversion (Figure 5F). The polarization voltage of the second discharge plateau increases by about 18 mV from the 5th to 40th cycle and by 18 mV from the 40th to 80th cycle. The slowly increased polarization indicates that the amount of active Li is sufficient to support the stable cycle of the Li-S pouch cell due to the alleviated parasitic reactions.

The cycled Li-S pouch cells were disassembled after 103 cycles to evaluate the parasitic reactions on the Li metal anode. Specifically, it is a pioneering report of an evaluation on a cycled pouch cell under harsh test conditions after more than 100 cycles, which provides first-hand knowledge for further research. The core of the pouch cell is slightly wet and no dead Li attaches to the separator (Figure 6A). There is a large amount of residual Li on the copper (Cu) current collector although the distribution is uneven considering the repeated cycles (Figure 6B). Different regions (R₁ and R₂) of the Li metal anode were analyzed by scanning electron microscope (SEM). There is partial active Li in the incompact R₁ with some sunken pits (Figure 6C). The Li deposition in R₂ is much denser without enormous dead Li (Figure 6D), which differs from the mossy and dendritic Li cycled in routine ether-based electrolyte reported in the previous works.^{5,46,48} A stripping test of residual active Li was conducted by cycled Li | Cu cells (Figure 6E). The amounts of residual active Li in R₁ and R₂ are about 6.5 and 9.9 mAh cm⁻², respectively, accounting for 32.5% and 49.5% retention of the amount of pristine active Li (100 μm, ~20 mAh cm⁻² based on double layers). The S-containing species on cycled Li in the pouch cell are detected by XPS. During the 160 s sputtering, only slight amounts of SO₄²⁻ and SO₃²⁻ are detected on the top layer of the SEI. Li₂S and Li₂S₂ are the main components in the whole SEI in S 2p spectra, corresponding to the results in the optical tests and coin cells (Figures 1D and 3D). The above evaluation demonstrates that the parasitic reactions between LiPSs and Li metal anodes are mitigated by DIPS-EPSE, which supports the long cycles of Li-S pouch cells. Furthermore, a pouch cell (2.6 Ah, 394 Wh kg⁻¹)

based on the total mass of the whole pouch cell was demonstrated with DIPS-EPSE under high-loading S cathodes (7.3 mg cm^{-2}), ultrathin Li metal anodes ($75 \text{ }\mu\text{m}$), and lean electrolytes ($2.7 \text{ }\mu\text{L mg}_\text{S}^{-1}$), proving that DIPS-EPSE can achieve practical high-energy-density Li-S pouch cells (Figure S15).

DISCUSSION

An EPSE is proposed to mitigate the parasitic reactions between the LiPS electrolyte and Li metal anodes based on the molecular-level solvation structure design of LiPSs. The unstable solvent shells around LiPSs in the routine DOL/DME electrolyte are the inducement for the parasitic reactions of LiPSs on Li metal anodes. In the EPSE, DIPS with a poor solvating power is recruited in the outer solvent shell of centered LiPSs. The high reduction stability of DIPS improves the reduction stability of the encapsulated LiPSs. Meanwhile, the inner solvent shell dominated by DME maintains satisfactory conversion kinetics of the S cathode. Low solvating power and high reduction stability are two basic criteria to construct nano-heterogeneous solvent shells of the EPSE. A pouch cell (1.2 Ah) with practical conditions of limited Li metal anodes ($50 \text{ }\mu\text{m}$), high-loading S cathodes (6.1 mg cm^{-2}), and lean electrolytes ($2.7 \text{ }\mu\text{L mg}_\text{S}^{-1}$) delivers stable cycling within 103 cycles. The analysis of the cycled pouch cell further proves the effectiveness of the EPSE. The proposed concept of encapsulating LiPS electrolytes sheds new light on the rational regulation of the solvation structure of LiPSs for achieving high-energy-density and long-cycling Li-S batteries.

EXPERIMENTAL PROCEDURES

Resource availability

Lead contact

Further information and requests for resources should be directed to and will be fulfilled by the lead contact, Professor Qiang Zhang (zhang-qiang@mails.tsinghua.edu.cn).

Materials availability

This study did not generate new unique reagents.

Data and code availability

All data reported in this paper will be shared by the lead contact upon request.

This paper does not report original code.

Any additional information required to reanalyze the data reported in this paper is available from the lead contact upon request.

Raw materials

Li metal foils were purchased from China Energy Lithium Co., Ltd. 1,2-dimethoxyethane (DME, battery grade, DoDoChem), 1,3-dioxolane (DOL, battery grade, DoDoChem), di-isopropyl sulfide (DIPS, 99%, ALFA), lithium bis-(trifluoromethanesulfonyl) imide (LiTFSI, battery grade, DoDoChem), and LiNO_3 (99.99% metals basis, Aladdin) were used as purchased without purification.

The preparation of sulfur cathode

Sulfur (S) and carbon nanotubes (CNT) were mixed first with a weight ratio of 7:3. Then, the S/CNT composite was ball-milled with poly(vinylidene fluoride) (PVDF) binder (9:1, by wt.) in *N*-methyl pyrrolidone (NMP). The obtained slurry was casted onto aluminum (Al) foil and further dried for 12 h at 60°C . The S/C cathode was

then cut into disks with a diameter of 13.0 mm. The S content in the electrode was 63%. The S loading was 1.2 and 3.9 mg cm⁻² for coin cells. All materials were kept in an argon-filled glove box with O₂ and H₂O contents below 0.1 ppm.

The preparation of electrolytes

The routine electrolyte is composed of 1.0 M LiTFSI in DOL/DME (1:1, by vol.), which is denoted as DOL/DME. The DIPS-EPSE is composed of 1.0 M LiTFSI in DIPS/DOL/DME (1:2:2, by vol.). The electrolytes were prepared in an argon-filled glove box with O₂ and H₂O contents below 1.0 ppm.

Electrochemical measurements

Li | Li symmetric cells were assembled in standard 2032-coin cells. Li foil (600 μm), polypropylene (PP) separator (Celgard 2400), and 30 μL of electrolyte were used. Li-S batteries under mild conditions were assembled with a thick Li anode (600 μm), a low loading S cathode (1.1 mg cm⁻²), and 25 μL electrolyte without LiNO₃. Li-S batteries under practical conditions were assembled with an ultrathin Li anode (50 μm), a high-loading S cathode (3.9 mg cm⁻²), and electrolytes containing 2 wt.% LiNO₃. The cells were tested using a Neware battery cycler (CT-4008t, Shenzhen, China) at 25°C. The voltage range of Li-S batteries is 1.7–2.6 V. Li-S batteries under practical conditions were cycled at 0.1 C (1 C = 1,675 mA g⁻¹) after two activation cycles at 0.05 C.

For the shuttle current test, Li-S cells were galvanostatically charged to 2.9 V and then discharged potentiostatically to 2.90, 2.60, 2.45, 2.43, 2.40, 2.39, 2.38, 2.37, 2.36, 2.35, 2.34, 2.25, and 2.20 V step by step. The shuttle current was determined by the steady-state current at different potentiostatic voltages.

The immersion test of Li metal in different LiPS electrolytes

Li₂S and S (1:7, by mol.) were added into DOL/DME or DIPS-EPSE electrolyte to prepare the Li₂S₈-containing solutions. For the visual experiment, Li foils were immersed in 2.5 mL of DOL/DME or DIPS-EPSE electrolyte (both containing 1.0 M LiTFSI and 3.0 mM Li₂S₈) to assess the stability of the LiPS electrolyte with Li metal. For the *in situ* UV-vis spectroscopy test, Li foils were immersed in 0.8 mL of DOL/DME or DIPS-EPSE electrolyte (both containing 1.0 M LiTFSI and 1.0 mM Li₂S₈). The solutions were characterized using a UV-vis spectrometer (AvaSpec-ULS4096CL-EVO, Avantes, China). To exclude the effect of the SEI in shielding LiPSs, Li foils were first immersed into DOL/DME or DIPS-EPSE electrolyte containing 1.0 M LiTFSI but without LiPSs for 50 h. Then, the pretreated Li foil was transferred into 2.5 mL of DOL/DME electrolyte containing 1.0 M LiTFSI and 3.0 mM Li₂S₈.

Material characterizations

The morphologies of the Li metal anode were observed by scanning electron microscopy (SEM, JSM 7401F, JEOL Ltd., Japan) operated at 3.0 kV. Cycled Li anodes were disassembled from Li-S batteries and washed three times with DME solvent to remove residual electrolyte and dried in a glove box thoroughly. X-ray photoelectron spectroscopy (XPS) experiments were conducted on a scanning X-ray microprobe (Quantera SXM, ULVAC-PHI, Inc) operated at 250 kV with monochromated Al K_α radiation. The Ar⁺ sputtering rate is ~20 nm min⁻¹ calibrated on the SiO₂ surface for XPS depth-profiling. ⁷Li NMR spectra were recorded at 233.2 MHz using a JNM-ECA600 system at room temperature.

Li-S pouch cells

Li-S pouch cells ($7 \times 4 \text{ cm}^2$) were fabricated in a dry room with a dew point below -40°C . The S loading of the cathode is 6.1 or 7.3 mg cm^{-2} for each single side. Ultrathin Li foils (50 or 75 μm for each single side) and a low E/S ratio (2.7 $\mu\text{L mg}_\text{S}^{-1}$) were used. The cathodes and anodes (double layers with active materials) were stacked layer-by-layer with a PP separator. The pouch cell was tested at 0.025 C. The energy density is evaluated based on the following equation:

$$E = \frac{E_d}{m_{\text{Li}} + m_{\text{S}} + m_{\text{Cu}} + m_{\text{Al}} + m_{\text{sep}} + m_{\text{tap}} + m_{\text{ely}} + m_{\text{pack}}}$$

where E is the gravimetric energy density. E_d is the discharge energy at the first cycle. m_{Li} , m_{S} , m_{Cu} , m_{Al} , m_{sep} , m_{tap} , m_{ely} , and m_{pack} are the mass of Li anode, S cathode (S, carbon, and binder), Cu current collector, Al current collector, separator, tap, electrolyte, and package, respectively. For the 1.2 Ah pouch cell, the initial discharge energy is 2.6 Wh. The total mass of the battery core (Li anode, S cathode, Cu current collector, Al current collector, separator, and tap) is 3.9 g. The mass of the electrolyte is 4.1 g. The mass of the package is 2.1 g. The energy density based on the total mass of the pouch cell is 257 Wh kg^{-1} . The energy density based on the mass of the pouch cell deducting the mass of the package is 325 Wh kg^{-1} . For the 2.6 Ah pouch cell, the initial discharge energy is 5.59 Wh. The total mass of the battery core (Li anode, S cathode, Cu current collector, Al current collector, separator, and tap) is 5.9 g. The mass of the electrolyte is 6.2 g. The mass of the package is 2.1 g. The energy density based on the total mass of the pouch cell is 394 Wh kg^{-1} . The energy density based on the mass of the pouch cell deducting the mass of the package is 462 Wh kg^{-1} .

MD simulations

MD simulations were performed using the Large Scale Atomic/Molecular Massively Parallel Simulator (LAMMPS) code.⁴⁹ Two models with and without DIPS were constructed for each LiPS species (Li_2S_4 , Li_2S_6 , and Li_2S_8), i.e., with six models in total. Models with DIPS contain 572 DOL, 386 DME, 100 LiTFSI, 10 LiPSs, and 137 DIPS molecules, while those without DIPS contain 712 DOL, 483 DME, 100 LiTFSI, and 10 LiPS molecules. The solvent force field parameters were generated by LigParGen web server,⁵⁰ except for that restrained electrostatic potential (RESP) atomic partial charges were assigned to each atom, which was obtained based on electrostatic potential (ESP) charges using Multiwfn program.⁵¹ The parameters for Li^+ , TFSI^- , and S_x^{2-} ($x = 4, 6$, and 8) were obtained from Jensen et al.,⁵² Koddermann et al.,⁵³ and Rajput et al.,³² respectively. The initial atomic coordinates were generated with Packing Optimization for Molecular Dynamics Simulations (Packmol)⁵⁴ program and the final constructions were visualized by VESTA⁵⁵ and VMD.⁵⁶

The time step was fixed to be 1 fs for all simulations. All systems were first equilibrated in isobaric-isothermal (NPT) ensemble using the Parrinello-Rahman barostat⁵⁷ for 4 ns to maintain a temperature of 298 K and a pressure of 1 atm with time constants of 0.1 and 1 ps, respectively. Subsequently, the models were heated from 298 to 340 K for 2 ns and maintained at 340 K for 4 ns, followed by annealing from 340 to 298 K in 2 ns and equilibrated at 298 K in NPT ensemble for another 4 ns. A production run of 7 ns at 298 K in canonical (NVT) ensemble under Nose-Hoover thermostat^{58,59} were finally conducted. The last 5 ns NVT simulations were output every 1,000 steps and used for the radial distribution function (RDF) analyses.

SUPPLEMENTAL INFORMATION

Supplemental information can be found online at <https://doi.org/10.1016/j.chempr.2021.12.023>.

ACKNOWLEDGMENTS

This work was supported by the Beijing Municipal Natural Science Foundation (Z20J00043), the National Natural Science Foundation of China (22061132002 and 21825501), the Seed Fund of Shanxi Research Institute for Clean Energy (SXKYJF015), the Beijing Natural Science Foundation (JQ20004 and L182021), and the Tsinghua University Initiative Scientific Research Program.

AUTHOR CONTRIBUTIONS

Q.Z. and X.-Q.Z. conceived and designed the experiments. L.-P.H. assembled the coin cells and pouch cells. L.-P.H., X.-Q.Z., and B.-Q.L. performed the electrochemical measurements and characterizations. N.Y. and X.C. conducted the MD simulations and rationales. All authors participated in data analyses and discussions. L.-P.H., X.-Q.Z., B.-Q.L., J.-Q.H., and Q.Z. co-wrote the manuscript with input from all authors.

DECLARATION OF INTERESTS

The authors declare no competing interests.

Received: October 8, 2021

Revised: November 21, 2021

Accepted: December 29, 2021

Published: January 21, 2022

REFERENCES

1. Bruce, P.G., Freunberger, S.A., Hardwick, L.J., and Tarascon, J.M. (2011). Li-O₂ and Li-S batteries with high energy storage. *Nat. Mater.* 11, 19–29. <https://doi.org/10.1038/nmat3191>.
2. Manthiram, A., Fu, Y., Chung, S.H., Zu, C., and Su, Y.S. (2014). Rechargeable lithium-sulfur batteries. *Chem. Rev.* 114, 11751–11787. <https://doi.org/10.1021/cr500062v>.
3. Mikhaylik, Y.V., and Akridge, J.R. (2004). Polysulfide shuttle study in the Li/S battery system. *J. Electrochem. Soc.* 151, A1969–A1976. <https://doi.org/10.1149/1.1806394>.
4. Tikekar, M.D., Choudhury, S., Tu, Z., and Archer, L.A. (2016). Design principles for electrolytes and interfaces for stable lithium-metal batteries. *Nat. Energy* 1, 16114. <https://doi.org/10.1038/nenergy.2016.114>.
5. Cheng, X.-B., Yan, C., Huang, J.-Q., Li, P., Zhu, L., Zhao, L., Zhang, Y., Zhu, W., Yang, S.-T., and Zhang, Q. (2017). The gap between long lifespan Li-S coin and pouch cells: the importance of lithium metal anode protection. *Energy Storage Mater.* 6, 18–25. <https://doi.org/10.1016/j.ensm.2016.09.003>.
6. Zhang, Y., Heim, F.M., Song, N., Bartlett, J.L., and Li, X. (2017). New insights into mossy Li induced anode degradation and its formation mechanism in Li-S batteries. *ACS Energy Lett.* 2, 2696–2705. <https://doi.org/10.1021/acsenerylett.7b00886>.
7. Xiao, J., Li, Q.Y., Bi, Y.J., Cai, M., Dunn, B., Glossmann, T., Liu, J., Osaka, T., Sugiura, R., Wu, B.B., et al. (2020). Understanding and applying coulombic efficiency in lithium metal batteries. *Nat. Energy* 5, 561–568. <https://doi.org/10.1038/s41560-020-0648-z>.
8. Hou, L.P., Zhang, X.Q., Li, B.Q., and Zhang, Q. (2021). Challenges and promises of lithium metal anode by soluble polysulfides in practical lithium-sulfur batteries. *Mater. Today* 45, 62–76. <https://doi.org/10.1016/j.mattod.2020.10.021>.
9. Gupta, A., Bhargav, A., and Manthiram, A. (2019). Highly solvating electrolytes for lithium-sulfur batteries. *Adv. Energy Mater.* 9, 1803096. <https://doi.org/10.1002/aenm.201803096>.
10. Bhargav, A., He, J.R., Gupta, A., and Manthiram, A. (2020). Lithium-sulfur batteries: attaining the critical metrics. *Joule* 4, 285–291. <https://doi.org/10.1016/j.joule.2020.01.001>.
11. Dörfler, S., Althues, H., Härtel, P., Abendroth, T., Schumm, B., and Kaskel, S. (2020). Challenges and key parameters of lithium-sulfur batteries on pouch cell level. *Joule* 4, 539–554. <https://doi.org/10.1016/j.joule.2020.02.006>.
12. Zhao, M., Li, B.Q., Zhang, X.Q., Huang, J.Q., and Zhang, Q. (2020). A perspective toward practical lithium-sulfur batteries. *ACS Cent. Sci.* 6, 1095–1104. <https://doi.org/10.1021/acscentsci.0c00449>.
13. Xin, S., Gu, L., Zhao, N.H., Yin, Y.X., Zhou, L.J., Guo, Y.G., and Wan, L.J. (2012). Smaller sulfur molecules promise better lithium-sulfur batteries. *J. Am. Chem. Soc.* 134, 18510–18513. <https://doi.org/10.1021/ja308170k>.
14. Su, Y.S., and Manthiram, A. (2012). Lithium-sulphur batteries with a microporous carbon paper as a bifunctional interlayer. *Nat. Commun.* 3, 1166. <https://doi.org/10.1038/ncomms2163>.
15. Yuan, Z., Peng, H.J., Hou, T.Z., Huang, J.Q., Chen, C.M., Wang, D.W., Cheng, X.B., Wei, F., and Zhang, Q. (2016). Powering lithium-sulfur battery performance by propelling polysulfide redox at sulfiphilic hosts. *Nano Lett.* 16, 519–527. <https://doi.org/10.1021/acs.nanolett.5b04166>.
16. Shi, Z.X., Li, M.T., Sun, J.Y., and Chen, Z.W. (2021). Defect engineering for expediting Li-S chemistry: strategies, mechanisms, and perspectives. *Adv. Energy Mater.* 11, 2100332. <https://doi.org/10.1002/aenm.202100332>.
17. Zheng, Z.J., Ye, H., and Guo, Z.P. (2021). Recent progress on pristine metal/covalent-organic frameworks and their composites for lithium-sulfur batteries. *Energy Environ. Sci.* 14, 1835–1853. <https://doi.org/10.1039/D0EE03181J>.
18. Zhang, Y., Liu, J., Wang, J., Zhao, Y., Luo, D., Yu, A., et al. (2021). Engineering oversaturated Fe-N₃ multifunctional catalytic sites for durable lithium-sulfur batteries. *Angew. Chem. Int. Ed.*

- Engl. 60, 26622–26629. <https://doi.org/10.1002/anie.202108882>.
19. Liu, Y., Elias, Y., Meng, J., Aurbach, D., Zou, R., Xia, D., and Pang, Q. (2021). Electrolyte solutions design for lithium-sulfur batteries. *Joule* 5, 2323–2364. <https://doi.org/10.1016/j.joule.2021.06.009>.
20. Suo, L., Hu, Y.S., Li, H., Armand, M., and Chen, L. (2013). A new class of solvent-in-salt electrolyte for high-energy rechargeable metallic lithium batteries. *Nat. Commun.* 4, 1481. <https://doi.org/10.1038/ncomms2513>.
21. Pang, Q., Shyamsunder, A., Narayanan, B., Kwok, C.Y., Curtiss, L.A., and Nazar, L.F. (2018). Tuning the electrolyte network structure to invoke quasi-solid state sulfur conversion and suppress lithium dendrite formation in Li-S batteries. *Nat. Energy* 3, 783–791. <https://doi.org/10.1038/s41560-018-0214-0>.
22. Zhao, C., Xu, G.L., Zhao, T.S., and Amine, K. (2020). Beyond the polysulfide shuttle and lithium dendrite formation: addressing the sluggish sulfur redox kinetics for practical high-energy Li-S batteries. *Angew. Chem. Int. Ed.* 59, 17634–17640. <https://doi.org/10.1002/anie.202007159>.
23. Dokko, K., Tachikawa, N., Yamauchi, K., Tsuchiya, M., Yamazaki, A., Takashima, E., Park, J.-W., Ueno, K., Seki, S., Serizawa, N., and Watanabe, M. (2013). Solvate ionic liquid electrolyte for Li-S batteries. *J. Electrochem. Soc.* 160, A1304–A1310. <https://doi.org/10.1149/2.111308jes>.
24. Yanagi, M., Ueno, K., Ando, A., Li, S., Matsumae, Y., Liu, J., Dokko, K., and Watanabe, M. (2020). Effects of polysulfide solubility and Li ion transport on performance of Li-S batteries using sparingly solvating electrolytes. *J. Electrochem. Soc.* 167, 070531. <https://doi.org/10.1149/1945-7111/ab7a81>.
25. Peng, H.J., Huang, J.Q., Liu, X.Y., Cheng, X.B., Xu, W.T., Zhao, C.Z., Wei, F., and Zhang, Q. (2017). Healing high-loading sulfur electrodes with unprecedented long cycling life: spatial heterogeneity control. *J. Am. Chem. Soc.* 139, 8458–8466. <https://doi.org/10.1021/jacs.6b12358>.
26. Steudel, R., and Chivers, T. (2019). The role of polysulfide dianions and radical anions in the chemical, physical and biological sciences, including sulfur-based batteries. *Chem. Soc. Rev.* 48, 3279–3319. <https://doi.org/10.1039/c8cs00826d>.
27. Li, Z., Jiang, H., Lai, N.-C., Zhao, T., and Lu, Y.-C. (2019). Designing effective solvent-catalyst interface for catalytic sulfur conversion in lithium-sulfur batteries. *Chem. Mater.* 31, 10186–10196. <https://doi.org/10.1021/acs.chemmater.9b03885>.
28. Li, Z.J., Zhou, Y.C., Wang, Y., and Lu, Y.C. (2019). Solvent-mediated Li₂S electrodeposition: A critical manipulator in lithium-sulfur batteries. *Adv. Energy Mater.* 9, 1802207. <https://doi.org/10.1002/aenm.201802207>.
29. Andersen, A., Rajput, N.N., Han, K.S., Pan, H., Govind, N., Persson, K.A., Mueller, K.T., and Murugesan, V. (2019). Structure and dynamics of polysulfide clusters in a nonaqueous solvent mixture of 1,3-dioxolane and 1,2-dimethoxyethane. *Chem. Mater.* 31, 2308–2319. <https://doi.org/10.1021/acs.chemmater.8b03944>.
30. Park, C., Ronneburg, A., Risse, S., Ballauff, M., Kanduć, M., and Dzubiella, J. (2019). Structural and transport properties of Li/S battery electrolytes: role of the polysulfide species. *J. Phys. Chem. C* 123, 10167–10177. <https://doi.org/10.1021/acs.jpcc.8b10175>.
31. Pascal, T.A., Wujcik, K.H., Wang, D.R., Balsara, N.P., and Prendergast, D. (2017). Thermodynamic origins of the solvent-dependent stability of lithium polysulfides from first principles. *Phys. Chem. Chem. Phys.* 19, 1441–1448. <https://doi.org/10.1039/c6cp06889h>.
32. Rajput, N.N., Murugesan, V., Shin, Y., Han, K.S., Lau, K.C., Chen, J., Liu, J., Curtiss, L.A., Mueller, K.T., and Persson, K.A. (2017). Elucidating the solvation structure and dynamics of lithium polysulfides resulting from competitive salt and solvent interactions. *Chem. Mater.* 29, 3375–3379. <https://doi.org/10.1021/acs.chemmater.7b00068>.
33. Cuisinier, M., Hart, C., Balasubramanian, M., Garsuch, A., and Nazar, L.F. (2015). Radical or not radical: revisiting lithium-sulfur electrochemistry in nonaqueous electrolytes. *Adv. Energy Mater.* 5, 1401801. <https://doi.org/10.1002/aenm.201401801>.
34. Zhang, G., Peng, H.J., Zhao, C.Z., Chen, X., Zhao, L.D., Li, P., et al. (2018). The radical pathway based on a lithium-metal-compatible high-dielectric electrolyte for lithium-sulfur batteries. *Angew. Chem. Int. Ed.* 57, 16732–16736. <https://doi.org/10.1002/anie.201810132>.
35. Diben, J.W., Smith, J.W., Zhou, N., Garcia-Araez, N., and Owen, J.R. (2016). Predicting the composition and formation of solid products in lithium-sulfur batteries by using an experimental phase diagram. *Chem. Commun.* 52, 12885–12888. <https://doi.org/10.1039/c6cc05881g>.
36. Barchasz, C., Molton, F., Duboc, C., Leprêtre, J.C., Patoux, S., and Alloin, F. (2012). Lithium/sulfur cell discharge mechanism: an original approach for intermediate species identification. *Anal. Chem.* 84, 3973–3980. <https://doi.org/10.1021/ac2032244>.
37. Zou, Q., and Lu, Y.C. (2016). Solvent-dictated lithium sulfur redox reactions: an operando UV-vis spectroscopic study. *J. Phys. Chem. Lett.* 7, 1518–1525. <https://doi.org/10.1021/acs.jpclett.6b00228>.
38. Han, K.S., Chen, J., Cao, R., Rajput, N.N., Murugesan, V., Shi, L., Pan, H., Zhang, J.-G., Liu, J., Persson, K.A., and Mueller, K.T. (2017). Effects of anion mobility on electrochemical behaviors of lithium-sulfur batteries. *Chem. Mater.* 29, 9023–9029. <https://doi.org/10.1021/acs.chemmater.7b02105>.
39. Kim, S., Jung, Y., and Lim, H.S. (2004). The effect of solvent component on the discharge performance of lithium-sulfur cell containing various organic electrolytes. *Electrochim. Acta* 50, 889–892. <https://doi.org/10.1016/j.electacta.2004.01.093>.
40. Chung, S.H., and Manthiram, A. (2019). Current status and future prospects of metal-sulfur batteries. *Adv. Mater.* 31, 1901125. <https://doi.org/10.1002/adma.201901125>.
41. Zhang, X.Q., Jin, Q., Nan, Y.L., Hou, L.P., Li, B.Q., Chen, X., et al. (2021). Electrolyte structure of lithium polysulfides with anti-reductive solvent shells for practical lithium-sulfur batteries. *Angew. Chem. Int. Ed.* 60, 15503–15509. <https://doi.org/10.1002/anie.202103470>.
42. Chen, X., Hou, T.-Z., Li, B., Yan, C., Zhu, L., Guan, C., et al. (2017). Towards stable lithium-sulfur batteries: mechanistic insights into electrolyte decomposition on lithium metal anode. *Energy Storage Mater.* 8, 194–201. <https://doi.org/10.1016/j.ensm.2017.01.003>.
43. Aurbach, D., Pollak, E., Elazari, R., Salitra, G., Kelley, C.S., and Affinito, J. (2009). On the surface chemical aspects of very high energy density, rechargeable Li-sulfur batteries. *J. Electrochem. Soc.* 156, A694–A702. <https://doi.org/10.1149/1.3148721>.
44. Zhang, S.S. (2012). Role of LiNO₃ in rechargeable lithium/sulfur battery. *Electrochim. Acta* 70, 344–348. <https://doi.org/10.1016/j.electacta.2012.03.081>.
45. Weller, C., Thieme, S., Härtel, P., Althues, H., and Kaskel, S. (2017). Intrinsic shuttle suppression in lithium-sulfur batteries for pouch cell application. *J. Electrochem. Soc.* 164, A3766–A3771. <https://doi.org/10.1149/2.0981714jes>.
46. Ye, G., Zhao, M., Hou, L.-P., Chen, W.-J., Zhang, X.-Q., Li, B.-Q., et al. (2022). Evaluation on a 400 wh kg⁻¹ lithium-sulfur pouch cell. *J. Energy Chem.* 66, 24–29. <https://doi.org/10.1016/j.jechem.2021.07.010>.
47. Niu, C.J., Liu, D.Y., Lochala, J.A., Anderson, C.S., Cao, X., Gross, M.E., Xu, W., Zhang, J.G., Whittingham, M.S., Xiao, J., and Liu, J. (2021). Balancing interfacial reactions to achieve long cycle life in high-energy lithium metal batteries. *Nat. Energy* 6, 723–732. <https://doi.org/10.1038/s41560-021-00852-3>.
48. Shi, L., Bak, S.-M., Shadike, Z., Wang, C., Niu, C., Northrup, P., Lee, H., Baranovskiy, A.Y., Anderson, C.S., Qin, J., et al. (2020). Reaction heterogeneity in practical high-energy lithium-sulfur pouch cells. *Energy Environ. Sci.* 13, 3620–3632. <https://doi.org/10.1039/D0EE02088E>.
49. Plimpton, S. (1995). Fast parallel algorithms for short-range molecular-dynamics. *J. Comput. Phys.* 117, 1–19.
50. Dodda, L.S., Cabeza de Vaca, I.C., Tirado-Rives, J., and Jorgensen, W.L. (2017). Ligargen web server: an automatic opsl-aa parameter generator for organic ligands. *Nucleic Acids Res.* 45, W331–W336. <https://doi.org/10.1093/nar/gkx312>.
51. Lu, T., and Chen, F.-W. (2012). Multiwfn: A multifunctional wavefunction analyzer. *J. Comput. Chem.* 33, 580–592. <https://doi.org/10.1002/jcc.22885>.
52. Jensen, K.P., and Jorgensen, W.L. (2006). Halide, ammonium, and alkali metal ion parameters for modeling aqueous solutions. *J. Chem. Theory Comput.* 2, 1499–1509. <https://doi.org/10.1021/ct600252r>.

53. Köddermann, T., Paschek, D., and Ludwig, R. (2007). Molecular dynamic simulations of ionic liquids: A reliable description of structure, thermodynamics and dynamics. *ChemPhysChem* 8, 2464–2470. <https://doi.org/10.1002/cphc.200700552>.
54. Martínez, L., Andrade, R., Birgin, E.G., and Martínez, J.M. (2009). Packmol: A package for building initial configurations for molecular dynamics simulations. *J. Comput. Chem.* 30, 2157–2164. <https://doi.org/10.1002/jcc.21224>.
55. Momma, K., and Izumi, F. (2011). Vesta 3 for three-dimensional visualization of crystal, volumetric and morphology data. *J. Appl. Crystallogr.* 44, 1272–1276. <https://doi.org/10.1107/S0021889811038970>.
56. Humphrey, W., Dalke, A., and Schulten, K. (1996). Vmd: visual molecular dynamics. *J. Mol. Graph.* 14, 33–38. [https://doi.org/10.1016/0263-7855\(96\)00018-5](https://doi.org/10.1016/0263-7855(96)00018-5).
57. Parrinello, M., and Rahman, A. (1981). Polymorphic transitions in single crystals: A new molecular dynamics method. *J. Appl. Phys.* 52, 7182–7190. <https://doi.org/10.1063/1.328693>.
58. Hoover, W.G. (1985). Canonical dynamics: equilibrium phase-space distributions. *Phys. Rev. A Gen. Phys.* 31, 1695–1697. <https://doi.org/10.1103/physrev.31.1695>.
59. Nosé, S. (1984). A molecular dynamics method for simulations in the canonical ensemble. *Mol. Phys.* 52, 255–268. <https://doi.org/10.1080/00268978400101201>.